ARTICLES

*Journal of Semiconductors*
(2023) 44, 122702
doi: 10.1088/1674-4926/44/12/122702

# Green synthesis of three-dimensional magnesium ferrite/titanium dioxide/reduced graphene from *Garcinia mangostana* extract for crystal violet photodegradation and antibacterial activity

**Tong Hoang Lin[1, 2, 3], Che Quang Cong[1, 2, 3], Nguyen Thanh Hoai Nam[1, 2, 3], Hoang An[1, 2, 3], Nguyen Duy Hai[1, 2, 3], Ton That Buu[1, 2, 3], Thoi Le Nhat Binh[1, 2, 3], Hoang Le Minh[1, 2, 3], Lam Thanh Ngan[1, 2, 3], Hoang Thuy Kim Ngan[1, 2, 3], Du Chi Vi[1, 2, 3], Ta Dang Khoa[2, 3], and Nguyen Huu Hieu[1, 2, 3, †]**

[1]VNU-HCM, Key Laboratory of Chemical Engineering and Petroleum Processing (Key CEPP Lab), Ho Chi Minh City University of Technology (HCMUT), 268 Ly Thuong Kiet Street, District 10, Ho Chi Minh City, Vietnam

[2]Faculty of Chemical Engineering, Ho Chi Minh City University of Technology (HCMUT), 268 Ly Thuong Kiet Street, District 10, Ho Chi Minh City, Vietnam

[3]Vietnam National University Ho Chi Minh City (VNU-HCM), Linh Trung Ward, Thu Duc City, Vietnam

**Abstract:** In this study, three-dimensional porous magnesium ferrite/titanium dioxide/reduced graphene oxide ($MgFe_2O_4$-GM/$TiO_2$/rGO (MGTG)) was successfully synthesized via green and hydrothermal-supported co-precipitation methods using the extract of *Garcinia mangostana* (*G. mangostana*) as a reducing agent. The characterization results indicate the successful formation of the nano/micro $MgFe_2O_4$ (MFO) and $TiO_2$ on the structure of the reduced graphene oxide (rGO), which can also act as efficient support, alleviating the agglomeration of the nano/micro MFO and $TiO_2$. The synergic effects of the adsorption and photodegradation activity of the material were investigated according to the removal of crystal violet (CV) under ultraviolet light. The effects of catalyst dosage, CV concentration, and pH on the CV removal efficiency of the MGTG were also investigated. According to the results, the CV photodegradation of the MGTG-200 corresponded to the pseudo-first-order kinetic model. The reusability of the material after 10 cycles also showed a removal efficiency of 92%. This happened because the materials can easily be recollected using external magnets. In addition, according to the effects of different free radicals $\cdot O_2^-$, $h^+$, and $\cdot OH$ on the photodegradation process, the photocatalysis mechanism of the MGTG was also thoroughly suggested. The antibacterial efficiency of the MGTG was also evaluated according to the inhibition of the Gram-positive bacteria strain *Staphylococcus aureus* (*S. aureus*). Concurrently, the antibacterial mechanism of the fabricated material was also proposed. These results confirm that the prepared material can be potentially employed in a wide range of applications, including wastewater treatment and antibacterial activity.

**Key words:** magnesium ferrite; titanium dioxide; reduced graphene oxide; *Garcinia mangostana*; photodegradation; antibacterial

**Citation:** T H Lin, C Q Cong, N T H Nam, H An, N D Hai, T T Buu, T L N Binh, H L Minh, L T Ngan, H T K Ngan, D C Vi, T D Khoa, and N H Hieu, Green synthesis of three-dimensional magnesium ferrite/titanium dioxide/reduced graphene from *Garcinia mangostana* extract for crystal violet photodegradation and antibacterial activity[J]. *J. Semicond.*, 2023, 44(12), 122702. https://doi.org/10.1088/1674-4926/44/12/122702

## 1. Introduction

Following the increasing demand of the pharmaceutical and textile industries, complex dyes and pigments have become more widespread, which has also had negative effects on the environment. Especially, in the process of dyeing fibers or fabrics, 10%–50% of untreated dyes are lost and discharged into the surroundings annually[1]. In addition, industrial wastewater contains large amounts of heavy metals, antibiotics, toxic organic substances, surfactants, and so on, which seriously affect the quality of the water sources (surface and groundwater), as well as the environment. In detail, due to the long-term accumulation of untreated industrial waste, the transmission of light is gradually reduced and this disrupts the biological activity of aquatic ecosystems, leading to the strong growth of molds and pathogenic bacteria in the water. Notably, if introduced into the human body through water, the dye molecules might gradually accumulate in the body, causing the inactivation of physiological functions of tissues and cells in the body, and lowering immunity translation of the human health system[2]. Among them, crystal violet (CV) is a common dye that is widely used in biological dyeing, dermatology, veterinary medicine, and dye processing. CV is a common industrial synthetic cationic dye and a member of the triphenylmethane family[3, 4]. Prolonged contact with CV dye leads to respiratory irritation, vomiting, diarrhea, headache, and dizziness. Prolonged exposure can also damage membranes mucus owing to the strong interaction

Correspondence to: N H Hieu, nhhieubk@hcmut.edu.vn
Received 28 JUNE 2023; Revised 4 AUGUST 2023.

between CV dye molecules and negatively charged cell membrane surfaces[3]. Therefore, there is an urgent requirement to find a method to handle exposure to CV dyes, in particular, and contaminated water remediation, in general.

Dye molecules composed of complex conjugated aromatic rings in wastewater are inert to light, heat, or oxidizing agents, and therefore decolorization is a puzzling problem[5]. Three kinds of pathways—chemical, physical, and biological—of treating contaminated dyed water have all been shown to be efficient. Various removal approaches have been used in the last few years, such as liquid film separation, biological treatment, oxidation, electrolysis, adsorption, chemical catalytic decomposition, ultrafiltration, desalination, and reverse osmosis[6–9]. Nevertheless, the electrochemical and membrane technologies require expensive equipment and conditioning to change the substances' system, whereas the chemical oxidation approach could be used or toxic chemicals (known as hazardous agents or secondary problems) could be released to the environment[10]. The remarkable characteristics of adsorbents (e.g. wide surface area, high sensitivity, higher accuracy, and low cost) have led to the growing use of the adsorption technique for pollutant removal. However, in addition to these benefits, this approach has serious concerns related to the treatment of the adsorption process and the reusability of the material, which limits the scope of their applications. Although this technique is believed to be constructive in removing organic and inorganic contaminants, it is tedious, expensive, requires high processing costs, and is often ineffective in removing fastidious compounds[11]. Therefore, these processes might occasionally remove harmful pollutants but they can also result in the production of undesired substances and health concerns. Photocatalytic decomposition is a method that is comparable and much more efficient than the other methods. This remedial technique, which has gained worldwide attention as the most functional, simple, practical, and non-toxic method, appears to be a promising strategy in the field of pollutant removal. When light approaches and excites the electron on the surface of the catalyst, they rapidly decolorize the textile dyes, using sunlight as an energy source and oxygen from the atmosphere as an oxidant. As a result, the toxic compounds are broken down into non-toxic chemical compounds or eventually become $CO_2$ and $H_2O$. Furthermore, the usage of renewable solar energy for lighting is another huge advantage, making this approach even more environmentally friendly[12].

The fabrication of photocatalysts with semiconductor properties is a promising pathway, specifically titanium dioxide ($TiO_2$). Thanks to the initial findings of Matsunaga *et al*. on the photocatalytic properties of titanium dioxide/platinum ($TiO_2$/Pt) materials under light excitation, the research on water disinfection, energy production, organic matter conversion, and pollutant decomposition of $TiO_2$ materials has been increasingly consolidated and expanded[13]. Moreover, with outstanding properties such as non-toxicity, affordable cost, chemical stability, and photochemical stability as compared to other semiconductor materials, the focus on environmental treatment in various applications is enabled thanks to the exhibited properties of $TiO_2$[12]. However, whether it exists alone or separately, $TiO_2$ exhibits many notable drawbacks, comprising a wide bandgap energy (~3.2 eV) and kinetically fast recombination of electron-hole pairs, along with poor affinity to organic dye molecules. In addition, due to its wide bandgap energy, $TiO_2$ only really exhibits strong photocatalytic activity in the ultraviolet (UV) irradiation region, leading to the limitations of $TiO_2$ in a lot of fields[12, 14]. In contrast, magnesium ferrite ($MgFe_2O_4$ (MFO)) is a known spinel ferrite material with unusual properties, such as magnetocrystalline anisotropy, moderate saturation magnetization, and resistance to optical corrosion in aqueous solution, and is able to absorb light in the visible region due to a low bandgap energy (~2.0 eV) and declining recombination rate of the electron–hole pairs[15]. Thus, doping $TiO_2$ with MFO enhances the photocatalytic activity of the binary composite and diminishes the drawback of each material when used alone. Therefore, the green synthesis of MFO using biochemical substances has emerged and has been used to reduce the number of hazardous chemicals discharged into the surroundings. Contemporarily, various types of plant extracts are being interested due to the facile, affordable, and eco-friendly synthesis process. In particular, the extract of *Garcinia mangostana* (*G. mangostana*) consists of a lot of secondary metabolites, such as tannin, xanthone, anthocyanin, total phenol, and so on[16]. Being basically weak, it can act as a mild reducing agent and stabilizer to prevent agglomeration during and after the formation of MFO nano- and microparticles[17, 18]. Moreover, the plant itself is abundant and widespread in multiple Asian regions. However, the binary composites still have a high recombination rate and are easy to be agglomerated[12, 19]. Herein, to tackle this situation, researchers have combined binary composites with carbon-based materials to facilitate electron movement. Among them, significantly, reduced graphene oxide (rGO) is considered to be a promising and outstanding material due to the physicochemical properties of graphene and graphene oxide (GO), which also can be easily synthesized from GO[20, 21]. The rGO material is synthesized from the self-assembly process of ordinary graphene sheets via van der Waals, π–π, and ionic bonds, or from the interactions between graphene sheets and binding agents (e.g. poly (vinyl alcohol), chitosan, stearic acid, etc.)[22, 23]. The porous 3D network facilitates the diffusion of pollutants, adsorption of toxic metals, and catalytic surface area, as well as providing efficient charge separation, all of which contribute to the applicable widespread of graphene-based materials[24]. The combination of $TiO_2$ and MFO decorated on the rGO framework is expected to be a potential approach due to reduced agglomeration of materials and enhanced charge–carrier separation, as well as the extended lifetime of the photogenerated electron–hole pair. Therefore, based on the three-dimensional structure, large surface area, and abundance of active sites of rGO materials, the adsorption capacity of dye molecules toxicity in the aquatic aqueous is also modified[25].

In this work, three-dimensional porous magnesium ferrite–titanium dioxide/reduced graphene oxide ($MgFe_2O_4$-GM/$TiO_2$/rGO (MGTG)) was fabricated via green and hydrothermal-supported co-precipitation methods using the extract of *G. mangostana* as reducing agent. The produced materials were thoroughly characterized via modern analytic methods, including field emission scanning electron microscopy (FE-SEM), energy-dispersive X-ray spectroscopy (EDX), Fourier-transform infrared spectroscopy (FTIR), X-ray diffraction

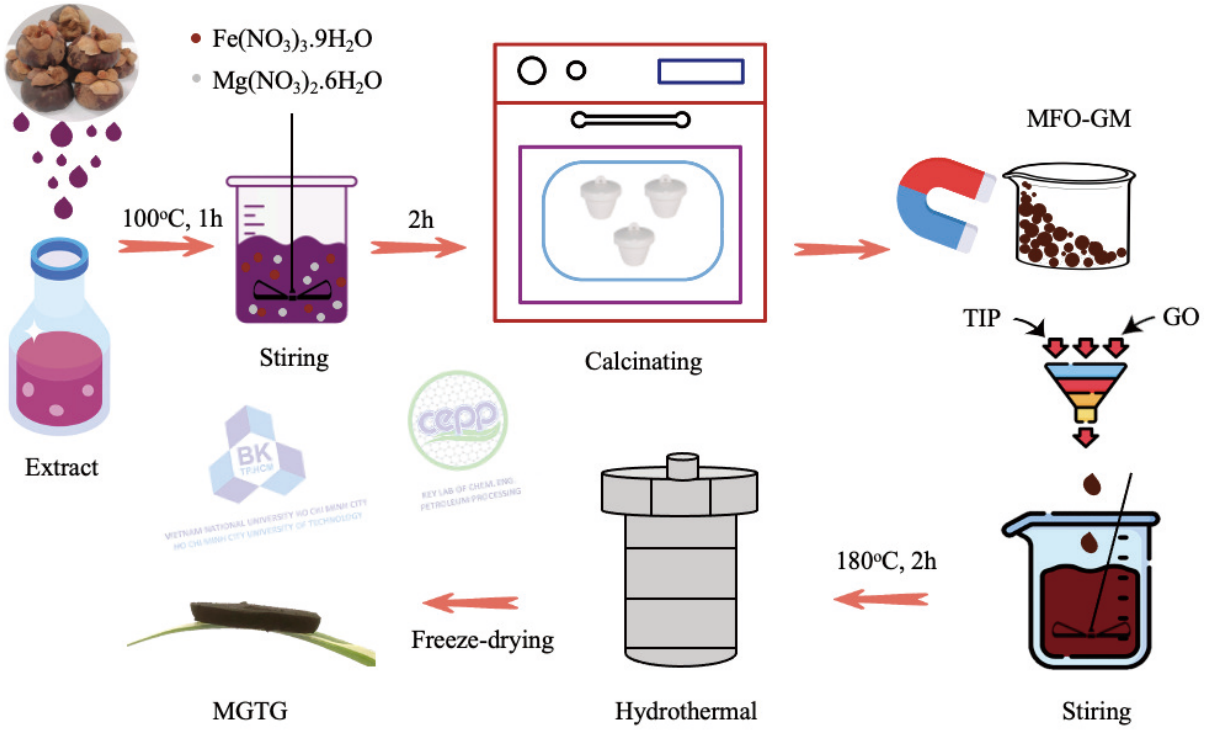


Fig. 1. (Color online) The synthesis procedure of MGTG material.

(XRD), ultraviolet–visible (UV–Vis) spectroscopy, Raman spectra, and thermogravimetric analysis (TGA). The electrochemical capability of the surveyed samples was also evaluated through, zeta potential (ZP) measurements, electrochemical impedance spectroscopy (EIS), and cyclic voltammetry (CVm) curve. The photocatalytic traits of the selected materials were then investigated regarding the degradation of CV under illumination. Additionally, the photodegradation process was also investigated with the pseudo-first-order kinetic model. Their antibacterial activities were studied against the Gram-positive bacterial strain *Staphylococcus aureus* (*S. aureus*) by measuring the inhibition zone diameter.

## 2. Materials and methods

### 2.1. Materials and chemicals

Graphite (particle size < 20 $\mu$m), titanium (Ⅳ) isopropoxide (TIP), and CV ($C_{25}H_{30}ClN_3$) were purchased from Sigma-Aldrich Co. Ltd., USA. Iron (Ⅲ) nitrate nonahydrate ($Fe(NO_3)_3{\cdot}9H_2O$), magnesium nitrate hexahydrate ($Mg(NO_3)_2{\cdot}6H_2O$), ammonium hydroxide ($NH_4OH$), sulfuric acid ($H_2SO_4$, 98%), phosphoric acid ($H_3PO_4$, 85%), potassium permanganate ($KMnO_4$), hydrogen peroxide ($H_2O_2$, 30%), polyvinylpyrrolidone (PVP), acetic acid ($CH_3COOH$), ethanol ($C_2H_5OH$), ethylenediamine tetraacetic acid disodium salt (EDTA), p-benzoquinone (BQ), and isopropanol (IPA) were purchased from Xilong Scientific Co. Ltd., China. All chemicals were utilized without further purification and double distilled water was used for all experiments.

### 2.2. Extraction of *G. mangostana* pericarp

*G. mangostana* pericarps were obtained from the Hoc Mon market, Viet Nam. The collected pericarps were carefully washed with distilled water before being dried at 60 °C and ground to collect a fine powder. After that, 10 g of powder was added to a 200 mL mixture of ethanol and distilled water (1 : 1) and heated to 90 °C for 1 h. The collected *G. mangostana* extract was then vacuum filtered to remove impurities and stored at 20 °C before utilization.

### 2.3. Synthesis of $MgFe_2O_4$ using extraction of *G. mangostana* pericarp reducing agent

MFO synthesized using *G. mangostana* pericarp extract (MFO-GM) nanocomposite was synthesized using the co-precipitation method. At first, 1.28 g $Mg(NO_3)_2{\cdot}6H_2O$ and 4.04 g $Fe(NO_3)_3{\cdot}9H_2O$ were dissolved in 100 mL of distilled water. The solution was then slowly added with 5 g PVP and 10 mL of $NH_4OH$, respectively, under stirring at 80 °C for 2 h. After that, the product was centrifuged and rinsed with distilled water to collect the solid. Finally, the sample was calcinated at 600 °C for 2 h to collect the MFO-GM powder. The influence of calcination temperatures on the formation of MFO-GM was also examined at 400, 600, and 800 °C, corresponding to the MFO-GM-400, MFO-GM-600, and MFO-GM-800 samples, respectively.

### 2.4. Synthesis of MGTG

The MGTG material was synthesized via the hydrothermal method. Initially, GO was prepared using the modified Hummers' method[26]. A determined amount of MFO-GM was added with GO to form a suspension mixture and sonicated for 30 min. Then, a mixture of TIP : acetic acid : ethanol (volume ratio of 1 : 1 : 15) was added to the prepared suspension under sonication for 15 min. The obtained mixture was subsequently put in a Teflon autoclave and underwent the hydrothermal process at 180 °C for 2 h to form a hydrogel. Finally, the hydrogel was freeze-dried at −80 °C for 48 h to acquire MFO/$TiO_2$/rGO composite (MGTG). MFO-GM contents were also investigated from 100, 150, 200, 250, and 300 mg, corresponding to the MGTG-100, MGTG-150, MGTG-200, MGTG-250, and MGTG-300 samples, respectively. The synthesis procedure of MGTG materials is depicted in Fig. 1.

### 2.5. Characterization of materials

FE-SEM micrographs (Hitachi S4800, Japan) were obtained to investigate the morphology and structure of fabricated materials, while EDX spectra (Jeol JMS 6490, Japan) were also conducted to study their elemental compositions. To investigate the functional groups arising from the material surfaces, FTIR spectra (Bruker TENSOR-27, Germany) were recorded by the KBr-pellet method in the wavelength of 600 to 4000 $cm^{-1}$ with an accuracy of 0.1% T and resolution of 0.2 $cm^{-1}$. XRD diffractograms (Bruker XRD D8, Germany) were also acquired via $CuK_\alpha$ irradiation ($\lambda$ = 0.154 nm) at $2\theta$ = 0°–80° and a scanning rate of 2° $min^{-1}$. Meanwhile, TGA analyses (Thermo Plus TG-8120) were evaluated to determine the thermal behaviors of surveyed materials, in which 50 mg of each was heated over 20 to 800 °C with a temperature and airflow rates of 10 °C/min and 50 mL/min, respectively. In addition, Raman spectra (LabRam micro-Raman) were collected at the excitation wavelength of 632 nm using a He–Ne laser, whilst Zetasizer Nano (Malvern ZS90) was also utilized for zeta potential measurement.

Regarding electrochemical investigations, CVm and EIS curves of synthesized materials were performed similarly to previous research[27]. Specifically, 90% of MFO-GM powder and 10% of carbon black were mixed and dispersed in 10 mL ethanol to prepare a glass carbon electrode, serving as an electrode in a three-electrode system for electrochemical measurement.

### 2.6. Photocatalytic degradation of CV

To investigate the photocatalytic performance of MGTG, the material was subjected to the photodegradation of CV, a common industrial organic dye, under light irradiation. In particular, 100 mL of CV solution (30 mg/L) was added with 20 mg of MGTG and continuously stirred in the dark for 60 min to reach adsorption–desorption equilibrium, before being illuminated with two 11-W UV lamps for 80 min. After each 20-min of irradiation, 4 mL of the mixture was withdrawn, filtered with a 0.22 $\mu$m nylon filter, and quantified the residual CV concentration using UV–Vis spectroscopy at the wavelength of 587 nm. Subsequently, the photodegradation efficiency ($H$, %) was calculated according to Eq. (1):

$$H = \frac{A_o - A}{A_o} \times 100, \tag{1}$$

where $A_o$ and $A$ are the initial and final absorbances of the sample, respectively.

The photocatalytic kinetics were also examined based on the pseudo-first-order model in Eq. (2):

$$\ln\left(\frac{C}{C_o}\right) = -kt, \tag{2}$$

where $C_o$ and $C$ (mg/L) are the initial and residual CV concentrations, respectively; $k$ ($min^{-1}$) is the reaction rate constant, and $t$ (min) is the reaction time.

In addition, the reusability of MGTG was further evaluated for 10 reusing runs. After each cycle, the material was recovered via centrifugation, washed with ethanol and distilled water, and dried at 60 °C, before being utilized for the succeeding run.

### 2.7. Antibacterial activity

An agar disc diffusion assay was used to evaluate the antibacterial activity of two samples MFO-GM and MGTG. The antibacterial properties of the samples were analyzed through the measurement of the inhibition diameter zone. Accordingly, all equipment was sterilized by autoclave at 121 °C for 20 min before conducting the experiments. Growth inhibition assays were carried out to assess the bacteriostatic effect against *S. aureus* which is known to be a typical strain of Gram-positive. In addition, indicator organisms were multiplied in agar. The agar containing the indicator microorganisms was prepared and poured into a petri dish. After solidification, a well was generated by perforating a 5 mm well, and antibacterial activity was determined. The diameters of inhibition zones were measured in mm including similar welling diameters when excluding size[28].

## 3. Results and discussion

### 3.1. Characterization of materials

The morphology of the MFO-GM samples calcinated at different temperatures was examined via FE-SEM images in Fig. 2. As can be observed, the surface of all three MFO-GM materials is relatively rough, in which the particles are vastly agglomerated with various deformed shapes[29]. Among them, the MFO-GM-600 sample provides the most uniform particle size and distribution throughout its profile, as compared to the other two. This can be attributed to the suitable treatment at a high temperature, leading to the formation of MFO-GM particles with better particle size and structure. Nevertheless, a relatively large particle diameter of the sample calcinated at 400 °C can result from an insufficient calcination process, while a plausible explanation for the roughness of MFO-GM-800 may be due to an overly high calcination temperature, which efficiently eliminates hydroxyl and water molecules adsorbed on the material surface, yielding a porous structure (Fig. 2(c))[30]. In addition, regarding the MGTG-200 composite, the recorded micrograph illustrates the distinct rGO surface with numerous folds and wrinkles[31], as well as the successful incorporation of MFO-GM and $TiO_2$ nanoparticles without significantly altering the rGO sheets.

Furthermore, as can be witnessed in Fig. 3, the FTIR spectra of MFO-GM samples indicate several signals corresponding to oxygen-containing functional groups arising from the material surface. In particular, a strong peak located at 3400 $cm^{-1}$ can be attributed to the vibration of the hydroxyl (–OH) functional group whereas other noticeable peaks are recognized at 1650, 1490, and 1200 $cm^{-1}$, which can be ascribed to the O–H bending vibration[32]. It is also noticeable that all MFO-GM materials provide a broad absorption signal at around 500 $cm^{-1}$ resulting from the vibration of metal oxide bonds, namely Mg–O and Fe–O, thereby affirming the existence of magnesium and ferrite oxide nanoparticles within the composition[33]. In addition, it can be observed that the spectra of MFO-GM-400 and MFO-GM-600 were relatively identical whilst the signals experienced a slight decrease in intensity as the calcination temperature increased to 800 °C. This phenomenon can be explained within the range of 400–600 °C, raising the calcination temperature can lead to a more efficient formation of well-defined

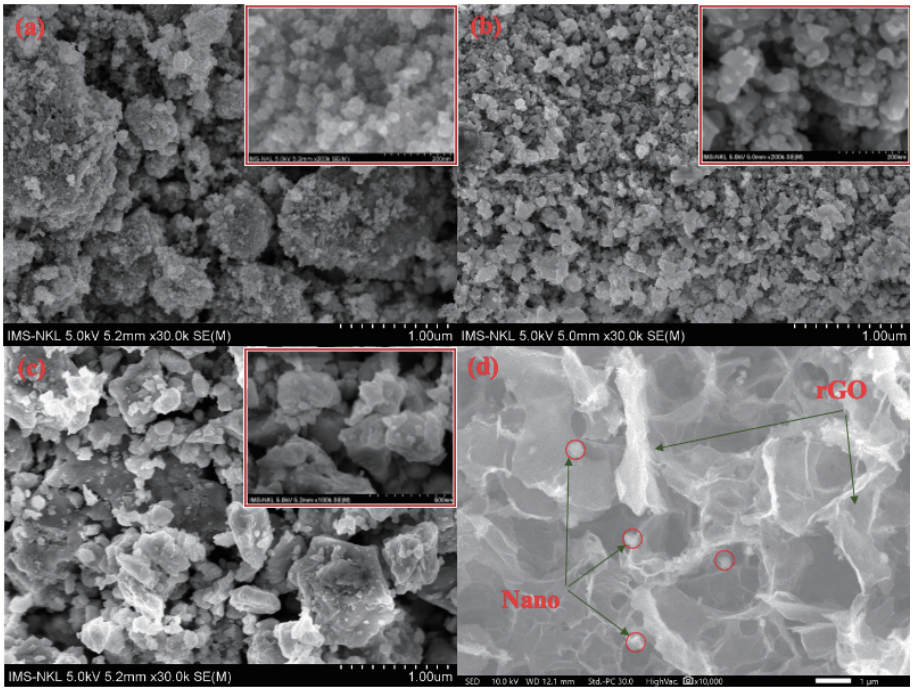


Fig. 2. (Color online) FE-SEM images of (a) MFO-GM-400, (b) MFO-GM-600, (c) MFO-GM-800, and (d) MGTG-200.

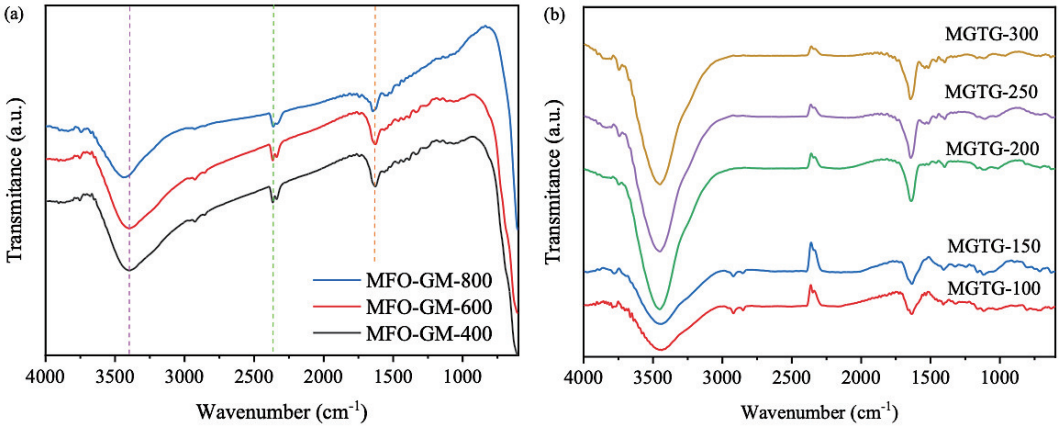


Fig. 3. (Color online) FTIR spectra of (a) MFO-GM and (b) MGTG materials.

nanoparticles. However, at elevated temperatures, thermal degradation of major constituents occurs, causing immense defective sites and decreasing the crystallinity of the nanocomposite[34], which is highly consistent with the FE-SEM images. Meanwhile, the figures of MGTG composites showed significant similarities compared to the spectra of MFO-GM, thus revealing the presence of aforementioned functional groups upon the incorporation of $TiO_2$ and graphene, as well as implying the successful formation of the nanocomposite via hydrothermal processes. More specifically, raising the MFO-GM content from 100 to 300 mg enhanced the peak intensities of the MGTG, which may elucidate an exposure of more magnesium and ferrite nanoparticles upon the thermal treatment as the precursor amount increased, whilst an excessive dose of MFO-GM (300 mg) barely impacted the intensity of corresponding signals. Along with the obtained results, 600 °C was further validated to be the suitable calcination temperature for MFO-GM, and thus 200 mg of MFO-GM-600 was chosen for synthesizing the optimal MGTG-200 sample.

To affirm the crystallinity of the MFO-GM samples and MGTG-200, their XRD patterns were studied, as described in Fig. 4(a). Accordingly, the figures of the three pristine materials possess sharp and distinctive peaks at $2\theta$ = 30.1°, 35.7°, 43.2°, 53.9°, 57.3°, and 62.8°, assigning to the (220), (311), (400), (422), (511), and (440) crystal planes. These patterns are characteristics of the cubic spinel structure of $MgFe_2O_4$ with no other impurity traces and can be well-indexed with the reported data (JCPDS no. 88–1936)[35]. Moreover, the highest intensity peak at the (311) plane, which is considered to indicate the crystalline nature of MFO, elucidates the promoted crystallinity of the MFO-GM-600 compared to others, which is in good agreement with the FE-SEM images and FTIR spectra. In addition, the figure of the MGTG-200 also observes great similarities with that of the pristine sample, thereby confirming that the incorporation with the rGO layer does not significantly alter the spinel structure of MFO-GM-600. The structure of the MGTG-200 sample was alternatively investigated via the Raman spectrum, as displayed in Fig. 4(b). As can be observed, a single characteristic peak can be detected at 661 $cm^{-1}$, which can be ascribed to the $A_{1g}$ mode of the tetrahedral structure in MFO[36]. Another precursor, GA, may be responsible for two distinctive peaks located at 1315 and

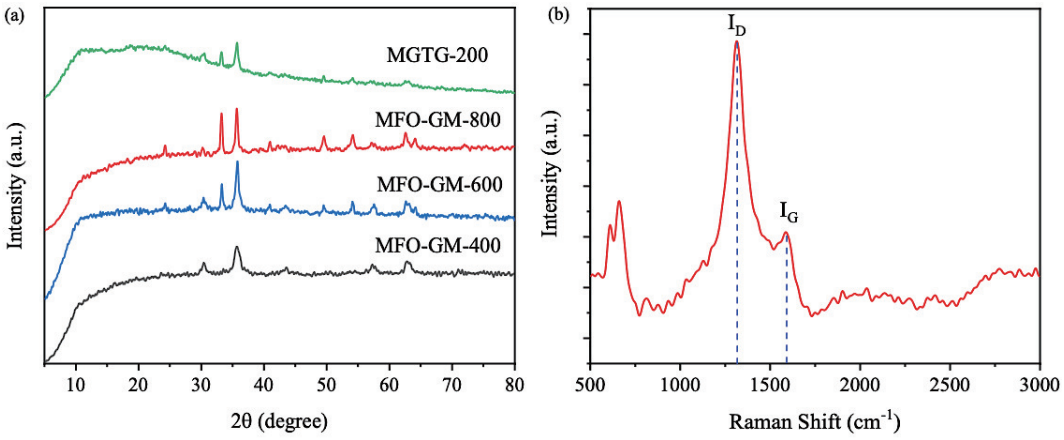


Fig. 4. (Color online) (a) XRD patterns of MFO-GM and MGTG-200 samples and (b) Raman spectrum of MGTG-200.

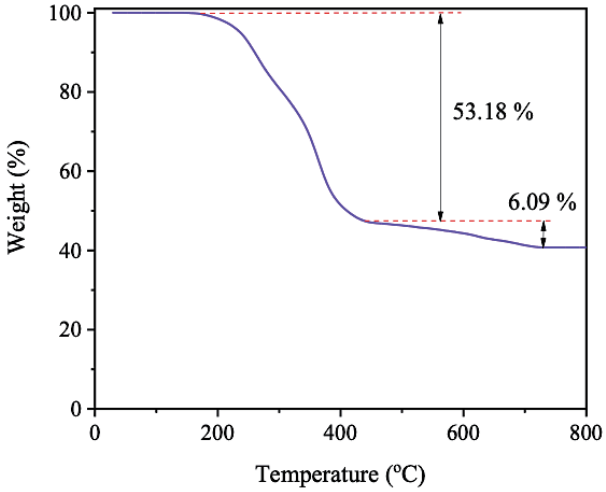


Fig. 5. (Color online) TGA curve of MGTG-200.

1589 cm$^{-1}$, corresponding to the D and G bands of the graphene-derived materials, respectively, with the dominant of the former shift[37]. Specifically, the D band reveals disorder structures in the material crystalline, while the latter is attributed to the vibration of $sp^2$-hybridized carbon atoms[38]. A relatively high-intensity ratio between the two ($I_D/I_G$) of MGTG-200 as compared to that of bare GA (1.27 versus 0.9, respectively) suggests an increment in disorder and defective sites of the GA interconnected structures upon the incorporation with MFO-GM and $TiO_2$. Regardless, the recorded spectrum indicates the signals of both MFO-GM and GA, hence affirming their successful combination to form the MGTG composite.

The thermal behavior of the MGTG-200 was scrutinized via the TGA curve, as indicated in Fig. 5. This figure endows several weight losses corresponding to different phase transitions and composition alternations of the nanocomposite with temperature. As can be seen, the first insignificant mass loss at 170 °C can be related to the evaporation of water molecules and minor organic traces on the material surface[39]. The second phase initiated at 320 °C resulted in a noticeable weight loss (53.18%), which can be assigned to the removal of leftover organic matters, as well as the incineration of unhydrolyzed TIP due to the rapid conversion of metallic hydroxides to their oxides[40]. Once the temperature reached 500 °C, there existed one more mass loss of 6.09%, which may correspond to the thermal decomposition of organic compounds in the material crystalline or structure of rGO. After the 600 °C mark, it was reported that the crystallization and phase transition of nanoparticles, particularly the formation of the spinel structure, has started despite no major alternation in the TGA curve[41], which is highly accordant with the FTIR results. In addition, beyond 700 °C, the curve remained constant at approximately 40% of the initial weight, showing that the coupling ferrites and other crystallines had been stably introduced.

The zeta potentials of the MGTG-200 and MFO-GM-600 are demonstrated in Fig. 6. These results indicate that both MGTG-200 and MFO-GM-600 are negatively charged. It is noteworthy that according to previous studies the absolute value of the zeta potentials higher than 25 mV indicated the great stability of the prepared material[42]. Regarding MGTG-200 and MFO-GM-600, the zeta potentials were determined to be −56.8 and −37.5 mV, respectively. The lower zeta potentials of the MFO-GM-600 also indicated the lower surface charge of the material when compared to the MGTG-200, revealing the higher probability of self-agglomeration between particles[43]. Additionally, the higher surface charge of the MGTG-200 also affirms the successful addition of rGO as this carbonaceous material possesses high zeta potential under neutral conditions, facilitating the uniform dispersion of the material in water[44].

The electrochemical behaviors of the MFO-GM-600 and MGTG-200 were also evaluated via the EIS and CV analysis, as indicated in Fig. 7. The results indicate that although both MFO-GM-600 and MGTG-200 possessed inconspicuous semicircles in the Nyquist plots, the slope of the straight region of the MGTG-200 within the range 350–700 Hz was slower than that of the MFO-GM-600, revealing the better electron transfer in the structure of the MGTG-200[45]. The results also indicate that the combination of different semiconductors such as MFO-GM-600, $TiO_2$, and rGO can effectively promote the charge transfer process, which accordingly reduces the resistance and enhances the photodegradation of organic dyes.

In addition, the electrochemical property of the MGTG-200 was also investigated via the CV curve within the potential window from 0 to 1.0 V with different scan rates. In particular, the CV curve of the MGTG-200 at the scan rate of 0.05–0.1 V·s$^{-1}$ is indicated in Fig. 7(b). As expected, the MGTG-200 sample possess a better electron transfer process

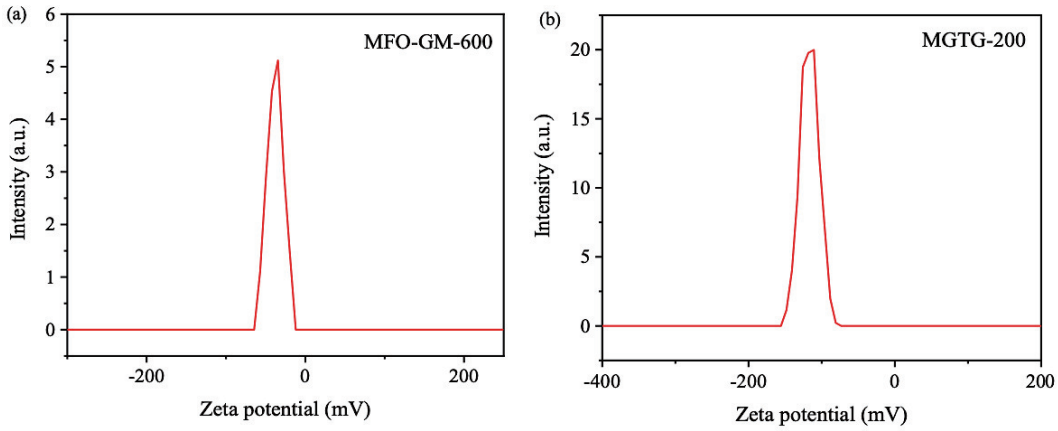


Fig. 6. (Color online) Zeta potential power spectra of (a) MFO-GM-600 and (b) MGTG-200.

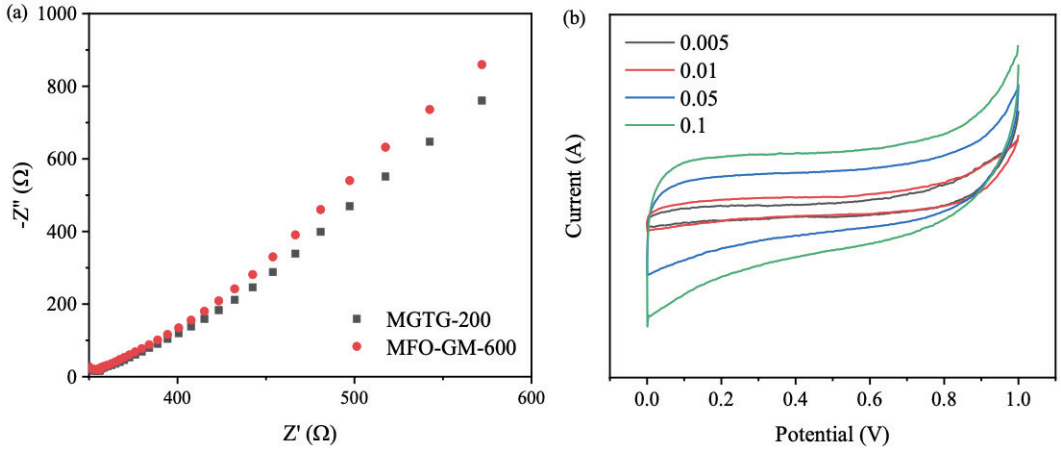


Fig. 7. (Color online) (a) EIS Nyquist and (b) CV curves of MGTG-200 at different scan rates.

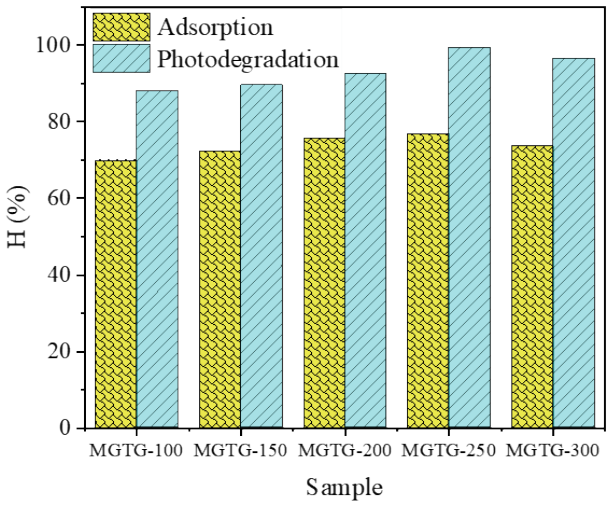


Fig. 8. (Color online) CV photodegradation yields of MGTG samples.

when the scan rate increased thanks to the synergic effects of the rGO and MFO, and $TiO_2$ nano/microparticles. The presence of a corrugated structure of the rGO sheets can also reduce the aggregation between nano- and micro-particles, and enhance the electron transport on the surface, eventually leading to enhanced electrochemical output[46].

### 3.2. Photocatalytic degradation of CV

The photocatalytic potential of synthesized materials was subsequently examined as the photodegradation of CV under light irradiation. According to the data in Fig. 8, upon the addition of $TiO_2$ and rGO, the adsorption and photodegradation efficiencies of all MGTG samples were improved noticeably as compared to those of the pristine MFO-GM-600. This can be ascribed to the incorporation of $TiO_2$ and rGO, which prolongs the recombination rate of the photogenerated electron-hole pairs, thereby enhancing the photocatalytic potential of the material[32, 47]. Additionally, with the introduction of a substrate such as rGO, the MFO and $TiO_2$ nanoparticles can be uniformly distributed and this reduces their agglomeration, which provides smaller particle sizes that can more efficaciously interact with CV molecules[48]. In addition, it is noteworthy that increasing the MFO-GM-600 dose in the MGTG resulted in a general increment in the CV photodegradation rate, especially the MGTG-200 with approximately 99.23% of CV elimination yield. Nevertheless, an overly-added amount of MFO-GM-600 (250 mg) caused a slight decrement in the photocatalytic efficiency of the MGTG-250, which can be attributed to the occupancy of MFO-GM-600 particles in the reactive sites of the rGO substrate, hampering the adsorption process and thus the photocatalytic activity towards the CV molecules[49]. The attained results are also well-accordant with the results of FTIR spectra.

The photocatalytic activity of the selected MGTG-200 sample was also investigated via the catalyst dose, CV concentration, and pH level. Regarding the catalyst dose, as can be witnessed in Fig. 9(a), it is noticeable that increasing the material dose up to 20 mg results in an increment in the CV elimination rate. This phenomenon is attributed to the

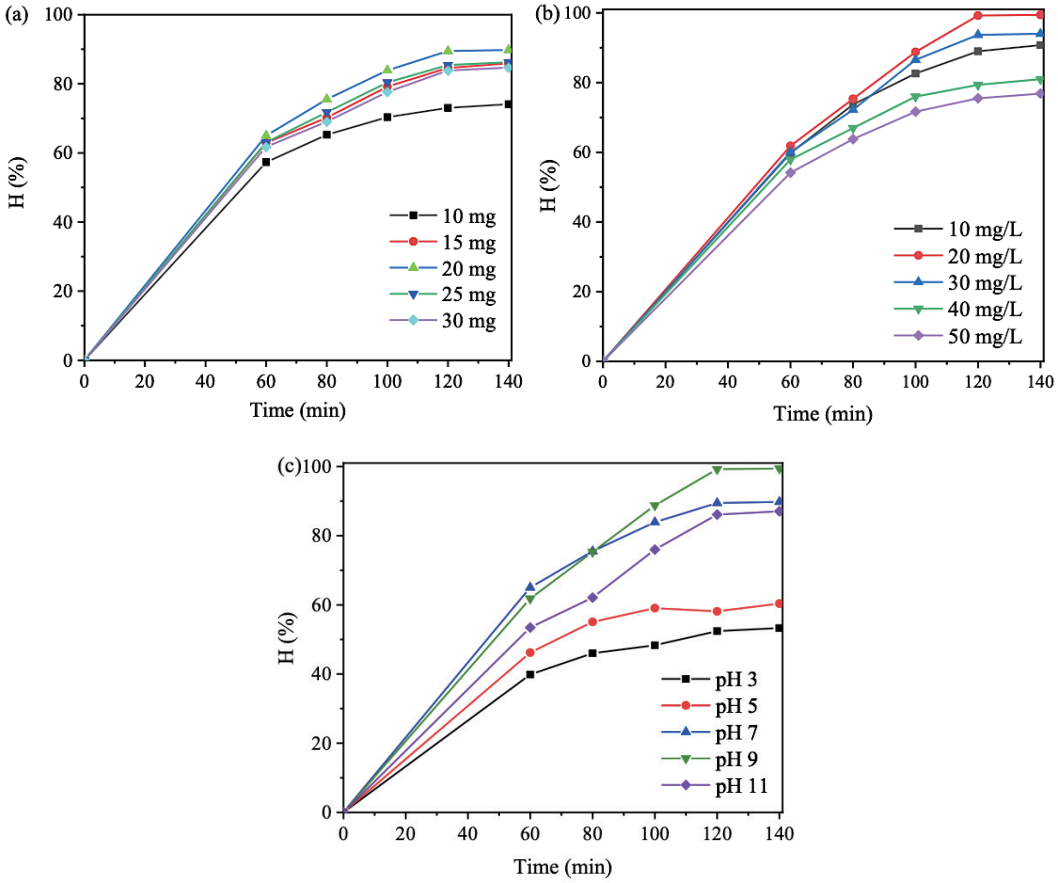


Fig. 9. (Color online) Effects of (a) catalyst dose, (b) pH level, and (c) CV concentration on the photocatalytic efficiency of MGTG-200.

increase in the available active sites thanks to more catalysts being added, which promotes the interaction of the dye molecules with the material, thereby enhancing the photodegradation efficiency. However, an excessive dose of MGTG-200 (25 and 30 mg) causes a slight drop in the reaction rate, which can be ascribed to an over-adsorption of CV onto the catalyst surface. Another explanation for this converse trend may be the increment in the mixture turbidity, which lowers the light transmittance to the material surface and consequently the photocatalytic activity[50].

The photocatalytic rate of the material was also promoted as the solution turns more basic (Fig. 9(b)). In particular, upon a pH increase from 3 to 9, the CV removal efficiency significantly improved, reaching 99.23% of degradation after 120 min of illumination. This phenomenon can be correlated to the photocatalytic mechanism, in which reactive oxygen radicals (ROS) such as hydroxyl radical (•OH), superoxide radical ($\bullet O_2^-$), or the photogenerated hole ($h^+$), participated in the elimination of contaminants, which can be easily produced thanks to the presence of $OH^-$ in basic media[51], hence exhibiting a superior photodegradation rate. Nonetheless, since CV is a cationic dye, a notably high pH level of 11 would result in a decreased photocatalytic efficiency due to the attraction of dye molecules with $OH^-$ instead of the MGTG-200 surface.

The initial dye concentration itself is also among the crucial factors influencing the photocatalytic efficiency of MGTG-200. According to Fig. 9(c), raising the CV concentration from 10–0 mg/L endows a better removal efficiency, whilst higher initial dye concentrations (30–50 mg/L) provide a converse effect. This can be assigned to the limited quantity of active sites from the MGTG-200 material despite changes in the treated CV concentration, making additional competition of dye molecules for available active sites[52]. In addition, similar to the case of catalyst dose, more CV added causes an increment in the turbidity of the solution, which efficaciously hinders the dye elimination yield. Therefore, the optimal conditions for the CV photodegradation experiment were determined at 20 mg of catalyst dose, pH 9, and 20 mg/L of dye concentration.

Moreover, the CV photodegradation activity of the MGTG-200 catalyst was also assessed via the kinetic regression model of the pseudo-first-order reaction. The experiments were performed at the selected optimal conditions, in which all data points locate surrounding the regression line, indicating great accuracy. As can be seen in Fig. 10(a), the correlation coefficient $R^2$ of the kinetic examination is also remarkably high (0.9946), thus alternatively confirming that the CV elimination process catalyzed by the synthesized MGTG-200 material follows pseudo-first-order kinetics. The recovery and reusability of the MGTG-200 are indicated in Fig. 10(b). According to the results, after 10 cycles of reusing, the removal efficiency of the material was still 92%, which may be due to the aid of the magnetic properties of the materials, which can improve the recovery efficiency. Moreover, the linearity of the efficiency decrement is in high sensed with a low reduction in the performance, indicating that the material is highly stable during consecutive cycles of CV elimination. According to these results, MGTG-200 can be potentially applied in the practical wastewater treatment process.

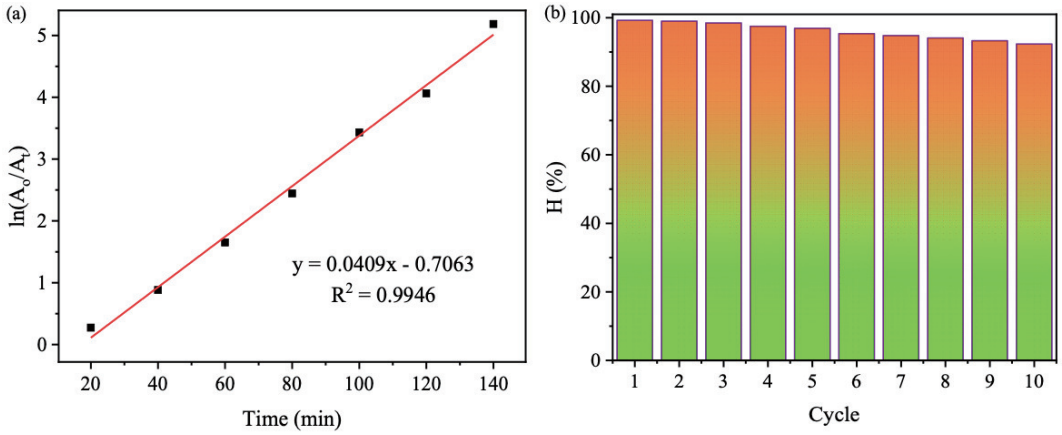


Fig. 10. (Color online) (a) Kinetic studies for the CV photodegradation and (b) recovery and reusability efficiency after 10 cycles of MGTG-200.

Table 1. CV photodegradation efficiency of several materials.

| No. | Materials | Catalyst dose (mg) | CV concentration (mg/L) | Reaction time (min) | Photodegradation rate (%) | References |
|---|---|---|---|---|---|---|
| 1 | MGTG-200 | 20 | 20 | 120 | 99.23 | This study |
| 2 | $CaCO_3$/g-$C_3N_4$ | 80 | 20 | 120 | 76 | [54] |
| 3 | SA-g-poly/ZnO/GO | 100 | 30 | 300 | 94 | [55] |
| 4 | $AgBiS_2$/g$C_3N_4$ | 30 | 20 | 60 | 71.81 | [56] |
| 5 | $KBiO_3$/g-$C_3N_4$ | 16 | 20 | 40 | 95 | [57] |

Table 1 provides the photocatalytic capability of several reported materials regarding the degradation of CV under irradiation. Accordingly, the fabricated MGTG-200 exhibited a relatively excellent photocatalytic property with nearly complete elimination of the dye after 120 min as compared to others. It is also noteworthy that the photocatalytic ability greatly depends on various factors, namely the distinguished natures of the catalyst and the dye, their concentrations, as well as the illumination power and time[53]. Along with the previously obtained results, the MGTG-200 material shows high potential for industrial treatment of dye-contaminated wastewater.

It should be noted that the CV photodegradation of the MGTG-200 under UV radiation solely relies on the generated ROS. Thus, the effects of different radical scavengers such as EDTA, BQ, and IPA were also investigated to evaluate the role of different free radicals such as $\cdot O_2^-$, $h^+$, and ·OH in the photodegradation process, respectively, as indicated in Fig. 11(a). According to the results, the participation of IPA led to a reduction in the removal efficiency from 99.23% to 80.26%, while the presence of EDTA and BQ reduced the efficiency to 59.18% and 49.38%, respectively. Thus, it can be concluded that the $\cdot O_2^-$ plays a main role in the CV photodegradation process of the MGTG-200.

The photocatalytic pathway of the MGTG material can be suggested similarly to previous research, which involves the transfer and recombination process of electron–hole ($e^-$–$h^+$) pairs[58]. As the material surface was irradiated, photo-induced $e^-$–$h^+$ pairs were generated, in which the formed electrons were subsequently transferred from the valence band of the pristine $MgFe_2O_4$ and $TiO_2$ to the conduction band, while the positive holes stayed structurally in the valence band of these nanoparticles. After that, the existing electrons in the conduction band once again traveled to the surface of rGO and participated in multiple reactions to generate ROS, such as $\cdot O_2^-$, ·OH, playing an exquisite role in the breakdown of CV into various benign degraded products. The proposed mechanism also proves the enhanced photocatalytic traits of the MGTG-200 as compared to that of the bare MFO-GM-600, which can be attributed to the incorporation of $TiO_2$ and rGO, effectively extending the recombination rate of electron–hole pairs, and thereby improving the photodegradation process of CV molecules[32, 47]. The whole photocatalysis scheme of MGTG-200 is described in Fig. 11(b) and Eqs. (3)–(9):

$$TiO_2 + h\nu \rightarrow TiO_2(e^- + h^+), \tag{3}$$

$$MgFe_2O_4 + h\nu \rightarrow MgFe_2O_4(e^- + h^+), \tag{4}$$

$$TiO_2(e^-) + MgFe_2O_4(e^-) + rGO \rightarrow rGO(e^-) + MgFe_2O_4 + TiO_2, \tag{5}$$

$$rGO(e^-) + O_2 \rightarrow \cdot O_2^- + rGO, \tag{6}$$

$$e^- + O_2 \rightarrow \cdot O_2^-, \tag{7}$$

$$h^+ + H_2O \rightarrow \cdot OH, \tag{8}$$

$$CV\ \ dye + ROS \rightarrow Degraded\ \ products. \tag{9}$$

### 3.3. Antibacterial activity

The antibacterial capability of the surveyed samples was recorded by measuring the inhibition zone diameter, as indicated in Fig. 12. As can be seen, regarding the MFO-GM materials, only the inhibitory zone of MFO-GM-400 and MFO-GM-800 were visible, whereas nearly no inhibition can be

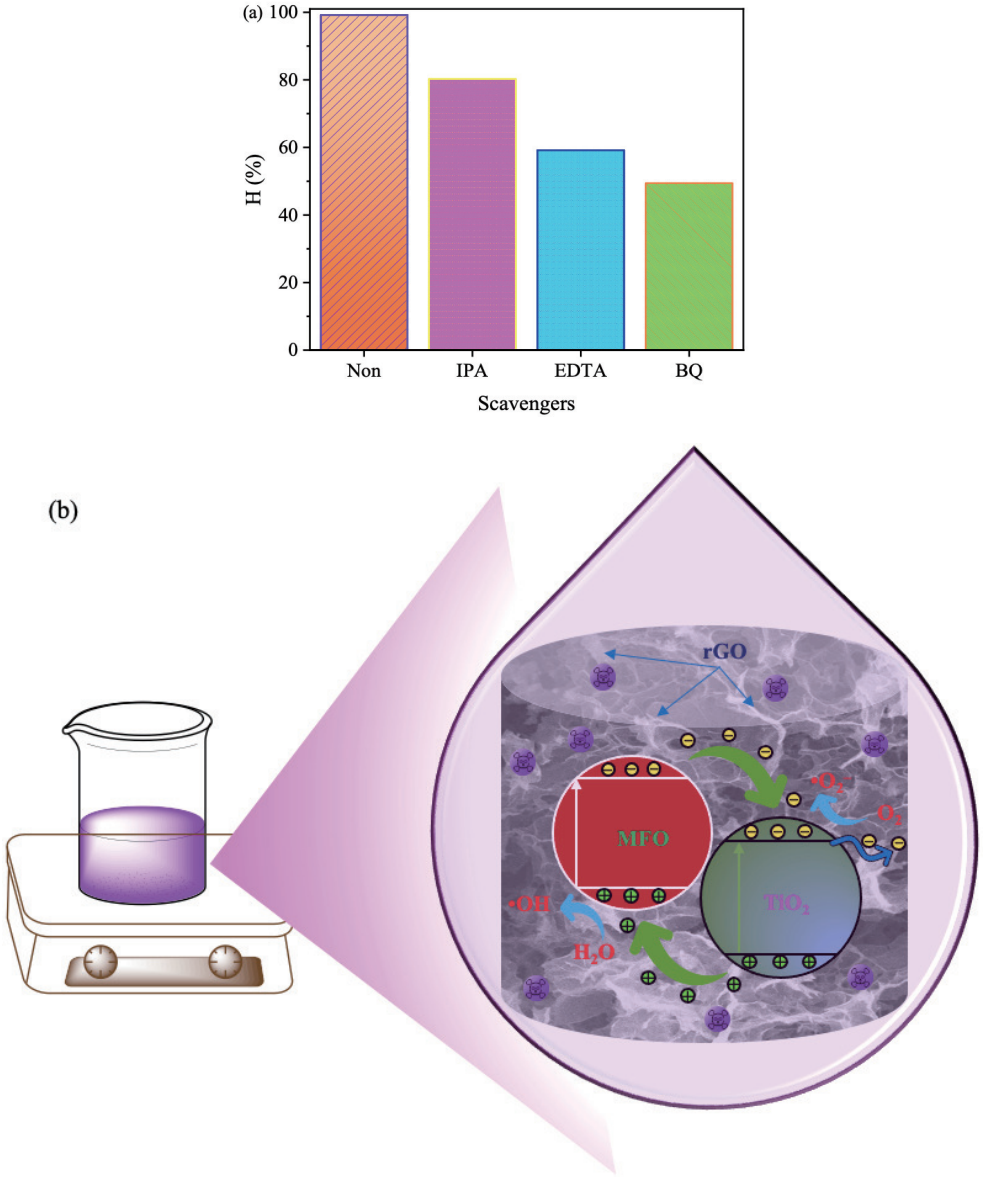


Fig. 11. (Color online) (a) Effects of radical scavengers on CV photocatalytic degradation under UV light and (b) photocatalytic scheme of the MGTG-200 material.

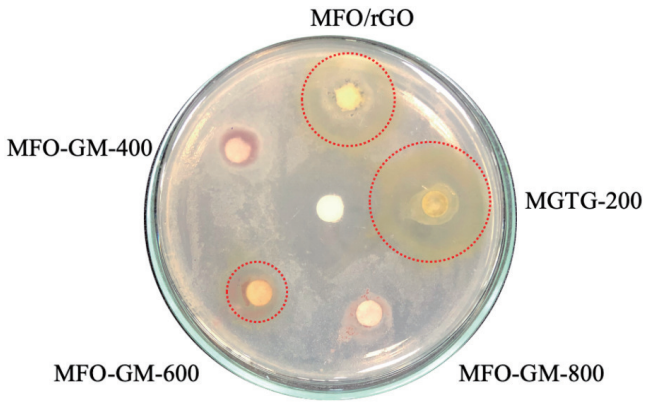


Fig. 12. (Color online) Inhibition zone diameter of surveyed materials against *S. aureus*.

observed for the other two. This phenomenon can result from the small particle sizes, as well as the high crystallinity of the former, which can facilitate an efficient interaction between the bacteria and material surface, exhibiting a higher bactericidal rate. Furthermore, the incorporation of rGO and additionally $TiO_2$ to form MFO/rGO and MGTG-200 led to a notable increment in the antibacterial efficiency against *S. aureus* with nearly 15.7 and 20 mm of inhibition zone diameters, respectively. This improvement can be attributable to the inherent moderate bactericidal activities of the pristine rGO, MFO, and $TiO_2$ precursors, which can increase the antibacterial capability of the composite as a whole[59–61]. Another plausible explanation is that similar to the case of photocatalytic assessment, without bonding to a substrate such as rGO, the bare MFO-GM-600 nanoparticles can be easily agglomerated, generating large particles and clusters, thus critically hindering the bactericidal activity[48]. Hence, the obtained results partially reveal that the MGTG-200 material has great bactericidal efficiency that may be potentially applied in the medical sector.

The inhibition zone diameters of reported materials are listed in Table 2 to further validate the antibacterial capability of the synthesized MGTG-200. In detail, the composite in this study provides a relatively good inhibitory diameter

Table 2. Inhibition zone diameter towards *S. aureus* of several materials.

| No. | Materials | Material concentration (mg/L) | Inhibition zone diameter (mm) | References |
|---|---|---|---|---|
| 1 | MGTG-200 | 10 | 20 | This study |
| 2 | Se-NPs | 62.5 | 12.2 | [63] |
| 3 | $Ag_2S$-ZnO/GO | 20 | 12 | [64] |
| 4 | $CeO_2$/g-$C_3N_4$ | 70 | 18.9 | [65] |
| 5 | ZnO/NiO/g-$C_3N_4$ | 400 | 17 | [66] |

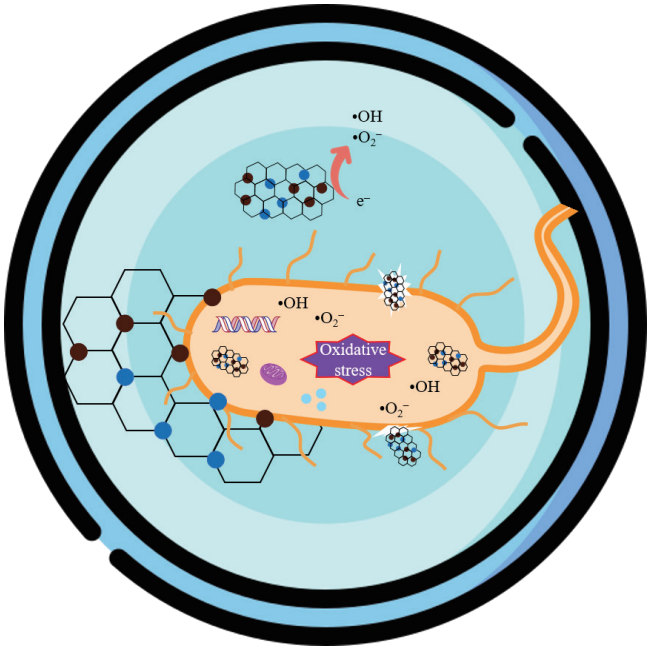


Fig. 13. (Color online) Antibacterial mechanism of the MGTG-200 material.

(20 mm) at a lower concentration (10 mg/L) as compared to the others, affirming a promising antibacterial property. Comparable to the photocatalytic traits, the bactericidal rate is strongly affected by the nature of the material and the treated bacterial strain, as well as the material concentration and particle size, which can impact the interaction pathway between the antibacterial agent with the bacterial cells[62]. Regardless, the combination of MFO-GM-600, $TiO_2$, and rGO to produce the MGTG-200 composite can be a promising candidate for multi-purpose material that possesses enhanced photocatalytic and antimicrobial characteristics.

As shown in Fig. 13, the proposed antibacterial scheme of the MGTG composite consists of several possible interactions. The MFO and $TiO_2$, similar to most metallic nanoparticles, can physically damage the bacterial cell membranes by penetrating or destroying the cellular barriers, thus hindering bacterial development[48]. Moreover, metallic fragments have also been reported to bind with bacterial internal organs or structures, which can interrupt their protein synthesis, electron transportation, or even cell division, thereby leading to the death of the whole bacterial population. Another bactericidal pathway is that MFO and $TiO_2$ nanoparticles can generate multiple ROS, whose excessive presence inside the cytoplasm may cause oxidative stress, resulting in the denaturation and thereby the annihilation of bacteria[67]. Meanwhile, rGO also endows a notable antibacterial capability, in which large graphene layers can enclose, isolate, and kill bacteria, while smaller ones serve as tiny blades and shear through the bacterial cell walls. Additionally, comparable to metallic particles, rGO can also produce ROS that initiates a series of redox reactions, and effectively impact and inhibit bacterial growth[68]. As a result, the incorporation of the three precursors to generate the MGTG-200 can greatly promote the bactericidal efficiency of the material.

## 4. Conclusions

In this study, the three-dimensional porous magnesium ferrite–titanium dioxide/reduced graphene oxide (MGTG) was successfully synthesized via green and hydrothermal-supported co-precipitation methods using the extract of *G. mangostana* as a reducing agent. The electrostatic interaction between $MgFe_2O_4$ and rGO plays a crucial role in the dispersion and embedment of the $MgFe_2O_4$ on the corrugated structure of the rGO. Furthermore, the synergic influences of the rGO and the nanoparticles also contribute to the enhancement of the CV photodegradation activity. The results also indicated that the MGTG-200 containing 200 mg MFO-GM-600 showed the highest CV removal efficiency of 99.23% under the following conditions: catalyst dosage of 20 mg, CV concentration of 20 mg/L, and pH 10. Compared to previous studies, the material provides competitive performance with high stability and recoverability with the CV removal efficiency of the material still reaching 92% after 10 cycles. Additionally, the photodegradation process of the material also obeys the pseudo-first-order kinetic model with the correlation coefficient $R^2$ = 0.9946. In addition, based on the evaluation of the effect of radical scavenging agents, the results also indicate that $\cdot O_2^-$ plays the most significant role in the photodegradation process of the material. Furthermore, the antibacterial efficiency of the MGTG-200 was also assessed against the Gram-positive *S. aureus* with an inhibition zone diameter of 20 mm. The antibacterial mechanism of the material was also proposed according to the oxidative stress and sharp-edge cutting effect. The results confirmed that the prepared material can be potentially employed in a wide range of applications, including wastewater treatment and antibacterial activity.

## Acknowledgments

We acknowledge Ho Chi Minh City University of Technology (HCMUT), VNU-HCM for supporting this study.

## References

[1] Rajagopal S, Paramasivam B, Muniyasamy K. Photocatalytic removal of cationic and anionic dyes in the textile wastewater by $H_2O_2$ assisted $TiO_2$ and micro-cellulose composites. Sep Purif Technol, 2020, 252, 117444

[2] Fatima B, Siddiqui S I, Rajor H K, et al. Photocatalytic removal of organic dye using green synthesized zinc oxide coupled cadmium tungstate nanocomposite under natural solar light irradiation. Environ Res, 2023, 216, 114534

[3] Rahmat M, Rehman A, Rahmat S, et al. Highly efficient removal of crystal violet dye from water by $MnO_2$ based nanofibrous mesh/photocatalytic process. J Mater Res Technol, 2019, 8, 5149

[4] Dargahi M, Masteri-Farahani M, Shahsavarifar S, et al. Microemulsion-mediated preparation of $Ce_2(MoO_4)_3$ nanoparticles for photocatalytic degradation of crystal violet in aqueous solution. En-

viron Sci Pollut Res, 2020, 27, 12047
[5] Sanakousar M F, Vidyasagar C C, Jiménez-Pérez V, et al. Efficient photocatalytic degradation of crystal violet dye and electrochemical performance of modified MWCNTs/Cd-ZnO nanoparticles with quantum chemical calculations. J Hazard Mater Adv, 2021, 2, 100004
[6] Chen Y A, Xiang Z Y, Wang D S, et al. Effective photocatalytic degradation and physical adsorption of methylene blue using cellulose/GO/$TiO_2$ hydrogels. RSC Adv, 2020, 10, 23936
[7] Spitaleri L, Nicotra G, Zimbone M, et al. Fast and efficient Sun light photocatalytic activity of Au_ZnO core–shell nanoparticles prepared by a one-pot synthesis. ACS Omega, 2019, 4, 15061
[8] Xie J A, Wen W, Jin Q, et al. $TiO_2$ nanotrees for the photocatalytic and photoelectrocatalytic phenol degradation. New J Chem, 2019, 43, 11050
[9] Chimupala Y, Phromma C, Yimklan S, et al. Dye wastewater treatment enabled by piezo-enhanced photocatalysis of single-component ZnO nanoparticles. RSC Adv, 2020, 10, 28567
[10] Zhang P, Xu J K, Wang X J, et al. The third generation of artificial dye-decolorizing peroxidase rationally designed in myoglobin. ACS Catal, 2019, 9, 7888
[11] Etman A S, Abdelhamid H N, Yuan Y Y, et al. Facile water-based strategy for synthesizing $MoO_{3-x}$ nanosheets: Efficient visible light photocatalysts for dye degradation. ACS Omega, 2018, 3, 2193
[12] Buu T T, Son V H, Nam N T H, et al. Three-dimensional ZnO-$TiO_2$/graphene aerogel for water remediation: The screening studies of adsorption and photodegradation. Ceram Int, 2023, 49, 9868
[13] Uyguner Demirel C S, Birben N C, Bekbolet M. A comprehensive review on the use of second generation $TiO_2$ photocatalysts: Microorganism inactivation. Chemosphere, 2018, 211, 420
[14] Giang N T H, Huy L G, Khoi V H, et al. Enhanced photocatalytic activity of titanium dioxide-doped graphene aerogel towards p-nitrophenol removal from aqueous solutions. Mater Technol, 2022, 37, 2445
[15] Yuan X Z, Wang H, Wu Y, et al. A novel $SnS_2$-$MgFe_2O_4$/reduced graphene oxide flower-like photocatalyst: Solvothermal synthesis, characterization and improved visible-light photocatalytic activity. Catal Commun, 2015, 61, 62
[16] Melia S, Novia D, Juliyarsi I, et al. The characteristics of the pericarp of garcinia mangostana (mangosteen) extract as natural antioxidants in rendang. IOP Conf Ser:Earth Environ Sci, 2019, 287, 012028
[17] Apriandanu D O B, Yulizar Y. CuO-bentonite-gold nanocomposites: Facile green preparation and their characterization. Mater Lett, 2021, 284, 128911
[18] Sari I P, Yulizar Y. Green synthesis of magnetite ($Fe_3O_4$) nanoparticles using *Graptophyllum pictum* leaf aqueous extract. IOP Conf Ser:Mater Sci Eng, 2017, 191, 012014
[19] Shahid M, Liu J L, Ali Z, et al. Photocatalytic degradation of methylene blue on magnetically separable $MgFe_2O_4$ under visible light irradiation. Mater Chem Phys, 2013, 139, 566
[20] Tarcan R, Todor-Boer O, Petrovai I, et al. Reduced graphene oxide today. J Mater Chem C, 2020, 8, 1198
[21] Ye N, Wang Z, Wang S, et al. Aqueous aggregation and stability of graphene nanoplatelets, graphene oxide, and reduced graphene oxide in simulated natural environmental conditions: Complex roles of surface and solution chemistry. Environ Sci Pollut Res, 2018, 25, 10956
[22] Jiao C L, Xiong J Q, Tao J, et al. Sodium alginate/graphene oxide aerogel with enhanced strength-toughness and its heavy metal adsorption study. Int J Biol Macromol, 2016, 83, 133
[23] Fu X G, Choi J Y, Zamani P, et al. Co–N decorated hierarchically porous graphene aerogel for efficient oxygen reduction reaction in acid. ACS Appl Mater Interfaces, 2016, 8, 6488
[24] Long S X, Wang H, He K, et al. 3D graphene aerogel based photocatalysts: Synthesized, properties, and applications. Colloids Surf A, 2020, 594, 124666
[25] Viet T, Phong H, Thinh D B, et al. Enhanced photodegradation toward graphene–based $MgFe_2O_4$–$TiO_2$: Investigation and optimization. Int J Hydrogen Energy, 2022, 47, 32092
[26] Alkhouzaam A, Qiblawey H, Khraisheh M, et al. Synthesis of graphene oxides particle of high oxidation degree using a modified Hummers method. Ceram Int, 2020, 46, 23997
[27] Duy P H A, Tu P M, Son T T, et al. A facile fabrication of zinc oxide-doped carbon aerogel by cellulose extracted from coconut peat and sodium alginate for energy storage application. J Appl Polym Sci, 2023, 140, e53837
[28] Dat N M, Huong L M, Cong C Q, et al. Green synthesis of chitosan-based membrane modified with uniformly micro-sizing selenium particles decorated graphene oxide for antibacterial application. Int J Biol Macromol, 2022, 220, 348
[29] Ushakov M V, Nithya V D, Rajeesh Kumar N, et al. X-ray diffraction, magnetic measurements and Mössbauer spectroscopy of $MgFe_2O_4$ nanoparticles. J Alloys Compd, 2022, 912, 165125
[30] Zhou L Y, Liu J X, Lu A M, et al. Controllable synthesis of cubic magnetic $MgFe_2O_4$ derived from MgFe-LDHs for efficient removal of methyl orange. Chem Eng J, 2022, 428, 131174
[31] Zeeshan M, Yalcin K, Sarac Oztuna F E, et al. A new class of porous materials for efficient $CO_2$ separation: Ionic liquid/graphene aerogel composites. Carbon, 2021, 171, 79
[32] Israr M, Iqbal J, Arshad A, et al. Multifunctional $MgFe_2O_4$/GNPs nanocomposite: Graphene-promoted visible light driven photocatalytic activity and electrochemical performance of $MgFe_2O_4$ nanoparticles. Solid State Sci, 2020, 110, 106363
[33] Muwafaq M, Safa P. Hydrothermal synthesis and electrochemical performance of GNPs-doped $MgFe_2O_4$ electrodes for supercapacitors. Solid State Ion, 2023, 391, 116107
[34] Fu L M, Chen H W, Wang K, et al. Oxygen-vacancy generation in $MgFe_2O_4$ by high temperature calcination and its improved photocatalytic activity for $CO_2$ reduction. J Alloys Compd, 2022, 891, 161925
[35] Kumar G M, Cho H D, Lee D J, et al. Elevating the charge separation of $MgFe_2O_4$ nanostructures by Zn ions for enhanced photocatalytic and photoelectrochemical water splitting. Chemosphere, 2021, 283, 131134
[36] Tiano A L, Papaefthymiou G C, Lewis C S, et al. Correlating size and composition-dependent effects with magnetic, mössbauer, and pair distribution function measurements in a family of catalytically active ferrite nanoparticles. Chem Mater, 2015, 27, 3572
[37] Zu Y Q, Zhao Y Q, Xu K Z, et al. Preparation and comparison of catalytic performance for nano $MgFe_2O_4$, GO-loaded $MgFe_2O_4$ and GO-coated $MgFe_2O_4$ nanocomposites. Ceram Int, 2016, 42, 18844
[38] Li J N, Yu Y L, Chen D H, et al. Hydrophilic graphene aerogel anodes enhance the performance of microbial electrochemical systems. Bioresour Technol, 2020, 304, 122907
[39] Shakir I, Sarfraz M, Ali Z, et al. Magnetically separable and recyclable graphene-$MgFe_2O_4$ nanocomposites for enhanced photocatalytic applications. J Alloys Compd, 2016, 660, 450
[40] Da Silva E P, Guilherme M R, Tenório-Neto E T, et al. sc$CO_2$-based synthesis of semi-crystalline $TiO_2$ nanoparticles: A rapid and direct strategy. Mater Lett, 2014, 136, 133
[41] Guerrero-Urbaneja P, García-Sancho C, Moreno-Tost R, et al. Glycerol valorization by etherification to polyglycerols by using metal oxides derived from MgFe hydrotalcites. Appl Catal A, 2014, 470, 199
[42] Jadhav S V, Kim B M, Lee H Y, et al. Induction heating and *in vitro* cytotoxicity studies of $MnZnFe_2O_4$ nanoparticles for self-controlled magnetic particle hyperthermia. J Alloys Compd, 2018, 745, 282
[43] Tang S Q, Moon S J, Park K H, et al. Feasibility of TEOS coated

$CoFe_2O_4$ nanoparticles to a GMR biosensor agent for single molecular detection. J Nanosci Nanotechnol, 2011, 11, 82
[44] Baskoro F, Wong C B, Kumar S R, et al. Graphene oxide-cation interaction: Inter-layer spacing and zeta potential changes in response to various salt solutions. J Membr Sci, 2018, 554, 253
[45] Vusa C S R, Berchmans S, Alwarappan S. Facile and green synthesis of graphene. RSC Adv, 2014, 4, 22470
[46] Yan J, Liu J P, Fan Z J, et al. High-performance supercapacitor electrodes based on highly corrugated graphene sheets. Carbon, 2012, 50, 2179
[47] Huy B T, Jung D S, Kim Phuong N T, et al. Enhanced photodegradation of 2, 4-dichlorophenoxyacetic acid using a novel $TiO_2$@$MgFe_2O_4$ core@shell structure. Chemosphere, 2017, 184, 849
[48] Dat N M, Cong C Q, Phuc N M, et al. Facile phytosynthesis of gold nanoparticles-doped graphene oxide using *Mangifera indica* leaf extract: Characterization, antibacterial activity, and catalytic reduction of organic dyes. Mater Today Sustain, 2022, 19, 100216
[49] Feng Q, Li S Y, Ma W H, et al. Synthesis and characterization of $Fe_3O_4$/ZnO-GO nanocomposites with improved photocatalytic degradation methyl orange under visible light irradiation. J Alloys Compd, 2018, 737, 197
[50] Alharthi F A, Ali Alghamdi A, Al-Zaqri N, et al. Facile one-pot green synthesis of Ag–ZnO Nanocomposites using potato peeland their Ag concentration dependent photocatalytic properties. Sci Rep, 2020, 10, 20229
[51] Kazeminezhad I, Sadollahkhani A. Influence of pH on the photocatalytic activity of ZnO nanoparticles. J Mater Sci: Mater Electron, 2016, 27, 4206
[52] Zhang D F, Zeng F B. Visible light-activated cadmium-doped ZnO nanostructured photocatalyst for the treatment of methylene blue dye. J Mater Sci, 2012, 47, 2155
[53] Kumar A. A review on the factors affecting the photocatalytic degradation of hazardous materials. Mater Sci Eng Int J, 2017, 1
[54] Lu P, Hu X L, Li Y J, et al. Novel $CaCO_3$/g-$C_3N_4$ composites with enhanced charge separation and photocatalytic activity. J Saudi Chem Soc, 2019, 23, 1109
[55] Mohamed S K, Hegazy S H, Abdelwahab N A, et al. Coupled adsorption-photocatalytic degradation of crystal violet under sunlight using chemically synthesized grafted sodium alginate/ZnO/graphene oxide composite. Int J Biol Macromol, 2018, 108, 1185
[56] Ajiboye T O, Oyewo O A, Marzouki R, et al. Synthesis of $AgBiS_2$/g$C_3N_4$ and its application in the photocatalytic reduction of Pb(II) in the matrix of methyl orange, crystal violet, and methylene blue dyes. Ceram Int, 2023, 49, 6149
[57] Zhang H, He J, Wu P, et al. Facile synthesis of Z-scheme $KBiO_3$/g-$C_3N_4$ Z-scheme heterojunction photocatalysts: Structure, performance, and mechanism. J Environ Chem Eng, 2022, 10, 107804
[58] Kaur J, Kaur M. Facile fabrication of ternary nanocomposite of $MgFe_2O_4$ $TiO_2$@GO for synergistic adsorption and photocatalytic degradation studies. Ceram Int, 2019, 45, 8646
[59] Guzel Kaya G, Aznar E, Deveci H, et al. Aerogels as promising materials for antibacterial applications: A mini-review. Biomater Sci, 2021, 9, 7034
[60] Vargas M A, Rodríguez-Páez J E. Amorphous $TiO_2$ nanoparticles: Synthesis and antibacterial capacity. J Non Cryst Solids, 2017, 459, 192
[61] Priya R S, Kumar E R, Balamurugan A, et al. Green synthesized $MgFe_2O_4$ ferrites nanoparticles for biomedical applications. Appl Phys A, 2021, 127, 538
[62] Chandrasekaran M, Kim K D, Chun S C. Antibacterial activity of chitosan nanoparticles: A review. Processes, 2020, 8, 1173
[63] Hashem A H, Khalil A M A, Reyad A M, et al. Biomedical applications of mycosynthesized selenium nanoparticles using penicillium expansum ATTC 36200. Biol Trace Elem Res, 2021, 199, 3998
[64] Khan A U, Arooj A, Tahir K, et al. Facile fabrication of novel $Ag_2S$-ZnO/GO nanocomposite with its enhanced photocatalytic and biological applications. J Mol Struct, 2022, 1251, 131991
[65] Shoran S, Chaudhary S, Sharma A. Photocatalytic dye degradation and antibacterial activities of $CeO_2$/g-$C_3N_4$ nanomaterials for environmental applications. Environ Sci Pollut Res, 2023, 30, 98682
[66] Dineshbabu N, Jayaprakash R N, Karuppasamy P, et al. Investigation on Tetracycline degradation and bactericidal properties of binary and ternary ZnO/NiO/g-$C_3N_4$ composites prepared by a facile co-precipitation method. J Environ Chem Eng, 2022, 10, 107368
[67] Othman N H, Alias N H, Shahruddin M Z, et al. Adsorption kinetics of methylene blue dyes onto magnetic graphene oxide. J Environ Chem Eng, 2018, 6, 2803
[68] Cacaci M, Martini C, Guarino C, et al. Graphene oxide coatings as tools to prevent microbial biofilm formation on medical device. Advances in Experimental Medicine and Biology. Springer International Publishing, 2019, 14, 21

**Tong Hoang Lin** received her Bachelor's degree in 2020 from Ho Chi Minh City University of Industry and Trade and her Master's degree in 2023 from Ho Chi Minh City University of Technology under the supervision of Assoc. Prof. Nguyen Huu Hieu. Her research focuses on graphene photocatalytic materials.

**Che Quang Cong** is currently studying and conducting research at the Key CEPP Laboratory in Chemical Engineering in Ho Chi Minh University of Technology, Viet Nam National University Ho Chi Minh City under the supervision of Assoc. Prof. Nguyen Huu Hieu. His research interests include nanomaterials in photocatalytic application using bio-mediation methodology.

**Hoang An** recently received his Bachelor's degree in chemical engineering from the Ho Chi Minh University of Technology, Viet Nam National University Ho Chi Minh City and currently pursues a Master's degree in the same institution under the supervision of Assoc. Prof. Nguyen Huu Hieu. His research interests include photocatalyst and composite material, and graphitic carbon nitride-based material.

**Nguyen Duy Hai** recently received his Bachelor's degree in chemical engineering from the Ho Chi Minh University of Technology, Viet Nam National University Ho Chi Minh City and is currently pursuing a Master's degree in the same institution under the supervision of Assoc. Prof. Nguyen Huu Hieu. His research interests include the fabrication of graphene-based nanocomposites for the application in catalysis, colorimetric detection, and antimicrobial activities.

**Ton That Buu** received his Bachelor's degree in 2021 from University of Science, Viet Nam National University Ho Chi Minh City and his Master's degree in 2023 from University of Technology under the supervision of Assoc. Prof. Nguyen Huu Hieu. His research focuses on graphene, photocatalytic materials.

**Lam Thanh Ngan** is currently studying and conducting research at the Key CEPP Laboratory in Chemical Engineering at Ho Chi Minh University of Technology, Viet Nam National University Ho Chi Minh City under the supervision of Assoc. Prof. Nguyen Huu Hieu. Her research interests include nanomaterials in photocatalytic application.

**Hoang Thuy Kim Ngan** is currently studying and conducting research at the Key CEPP Laboratory in Chemical Engineering at Ho Chi Minh University of Technology, Viet Nam National University Ho Chi Minh City under the supervision of Assoc. Prof. Nguyen Huu Hieu. Her research interests include nanomaterials in photocatalytic application.

**Ta Dang Khoa** received his doctoral degree from the Chemical Engineering Department, Universiti Teknologi PETRONAS, in 2012. He is currently associate professor in chemical engineering in Ho Chi Minh University of Technology, Viet Nam National University Ho Chi Minh City. His current research interests include adsorption materials and photodegradation materials.

**Nguyen Huu Hieu** received his doctoral degree from Chonbuk National University, Korea, in 2012. He is currently associate professor in chemical engineering in Ho Chi Minh University of Technology, Viet Nam National University Ho Chi Minh City. His current research interests include graphene aerogel, adsorption materials, photodegradation materials.